Cell Reports

Report

Structural changes in the SARS-CoV-2 spike E406W mutant escaping a clinical monoclonal antibody cocktail

Graphical abstract

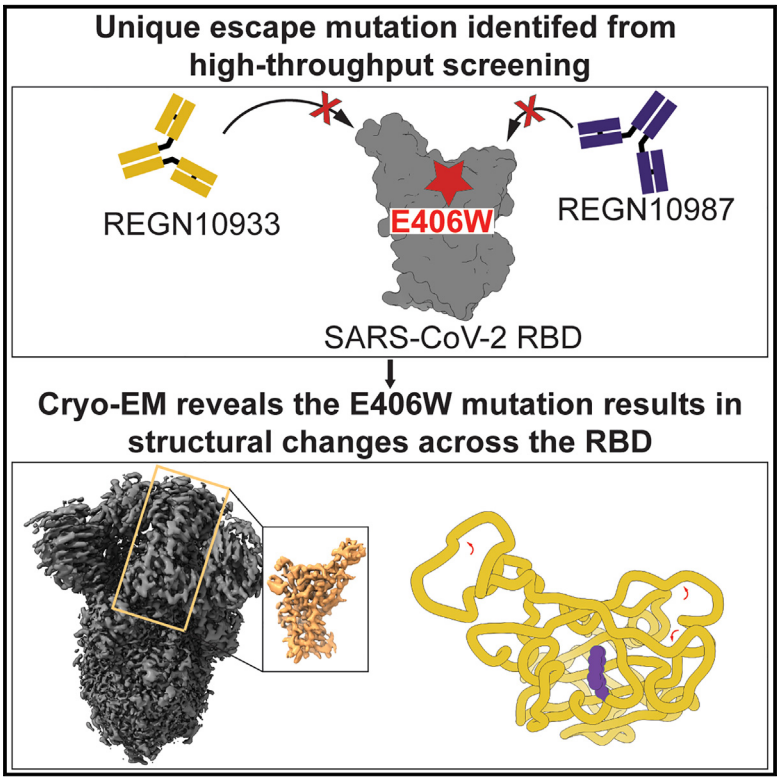

Highlights

- The SARS-CoV-2 spike E406W mutation remodels receptor-binding motif
- E406W-induced structural changes impact the epitopes of three monoclonal antibodies
- The remodeled E406W spike retains some, but not all, key contacts with the receptor, ACE2
- Vaccine-elicited sera have reduced potency against E406W spike pseudovirus

Authors

Amin Addetia, Young-Jun Park, Tyler Starr, ..., Davide Corti, Alexandra C. Walls, David Veesler

Correspondence

dveesler@uw.edu

In brief

Addetia et al. demonstrate that introduction of the E406W mutation in the SARS-CoV-2 spike protein causes widespread structural changes in the receptor-binding motif. These changes hinder the ability of three therapeutic antibodies to effectively bind the mutated spike protein.

Addetia et al., 2023, Cell Reports *42*, 112621
June 27, 2023
https://doi.org/10.1016/j.celrep.2023.112621

CellPress

Cell Reports

CellPress
OPEN ACCESS

Report

Structural changes in the SARS-CoV-2 spike E406W mutant escaping a clinical monoclonal antibody cocktail

Amin Addetia,[1,2] Young-Jun Park,[2,3] Tyler Starr,[3,4] Allison J. Greaney,[3] Kaitlin R. Sprouse,[2] John E. Bowen,[2] Sasha W. Tiles,[5] Wesley C. Van Voorhis,[5] Jesse D. Bloom,[3,4] Davide Corti,[6] Alexandra C. Walls,[2,3] and David Veesler[2,3,7,*]

[1]Molecular and Cellular Biology Graduate Program, University of Washington, Seattle, WA, USA
[2]Department of Biochemistry, University of Washington, Seattle, WA, USA
[3]Howard Hughes Medical Institute, Seattle, WA 98195, USA
[4]Basic Sciences Division, Fred Hutchinson Cancer Research Center, Seattle, WA 98109, USA
[5]Center for Emerging and Re-emerging Infectious Diseases, Division of Allergy and Infectious Diseases, Department of Medicine, University of Washington School of Medicine, Seattle, WA 98195, USA
[6]Humabs Biomed SA, a subsidiary of Vir Biotechnology, 6500 Bellinzona, Switzerland
[7]Lead contact
*Correspondence: dveesler@uw.edu
https://doi.org/10.1016/j.celrep.2023.112621

SUMMARY

Continued evolution of severe acute respiratory syndrome coronavirus 2 (SARS-CoV-2) is eroding antibody responses elicited by prior vaccination and infection. The SARS-CoV-2 receptor-binding domain (RBD) E406W mutation abrogates neutralization mediated by the REGEN-COV therapeutic monoclonal antibody (mAb) COVID-19 cocktail and the AZD1061 (COV2-2130) mAb. Here, we show that this mutation remodels the receptor-binding site allosterically, thereby altering the epitopes recognized by these three mAbs and vaccine-elicited neutralizing antibodies while remaining functional. Our results demonstrate the spectacular structural and functional plasticity of the SARS-CoV-2 RBD, which is continuously evolving in emerging SARS-CoV-2 variants, including currently circulating strains that are accumulating mutations in the antigenic sites remodeled by the E406W substitution.

INTRODUCTION

The receptor-binding domain (RBD) of the severe acute respiratory syndrome coronavirus 2 (SARS-CoV-2) spike glycoprotein is responsible for interacting with the host receptor ACE2 and initiating viral entry into cells.[1–3] The SARS-CoV-2 RBD is the target of the majority of neutralizing antibodies elicited by SARS-CoV-2 infection and COVID-19 vaccination, of virtually all vaccine-elicited cross-variant neutralizing antibodies, and of monoclonal antibodies (mAbs) used prophylactically or therapeutically.[4–9] Binding and neutralization of SARS-CoV-2 by individual mAbs can be escaped by single RBD residue mutations, which led to the development of therapeutic cocktails comprising two mAbs recognizing non-overlapping epitopes.[10–13] These cocktails have a higher barrier for the emergence of neutralization escape mutants than the individual constituting mAbs, as typically at least two distinct amino acid substitutions are required to evade neutralization by a two-mAb cocktail.

The REGEN-COV cocktail consists of two mAbs, casirivimab (REGN10933) and imdevimab (REGN10987), that bind non-overlapping RBD epitopes in the receptor-binding motif (RBM) and block ACE2 attachment.[12,13] We previously mapped all possible RBD residue mutations that permit escape from the REGEN-COV mAb cocktail and the COV2-2130 mAb, which led us to identify that the E406W substitution abrogated binding and neutralization of both REGEN-COV mAbs individually and the cocktail[10] as well as binding of COV2-2130.[14] Unexpectedly, residue E406 is located outside of the epitopes recognized by REGN10933, REGN10987, and COV2-2130, suggesting that this mutation might influence the overall structure of the RBD (presumably through an allosteric effect) while retaining detectable binding to dimeric human ACE2.[10]

RESULTS AND DISCUSSION

To understand the molecular basis of the E406W-mediated escape from the REGEN-COV cocktail and the COV2-2130 mAb, we characterized the SARS-CoV-2 spike (S) ectodomain trimer structure harboring the E406W mutation using single-particle cryoelectron microscopy. 3D classification of the dataset revealed the presence of two conformational states: one with three RBDs closed and one with one RBD open, accounting for approximately 70% and 30% of particles, respectively. We determined a structure of the closed S state at 2.3 Å resolution applying C3 symmetry (Figures 1 and S1; Table S1). Symmetry expansion, focused classification, and local refinement yielded

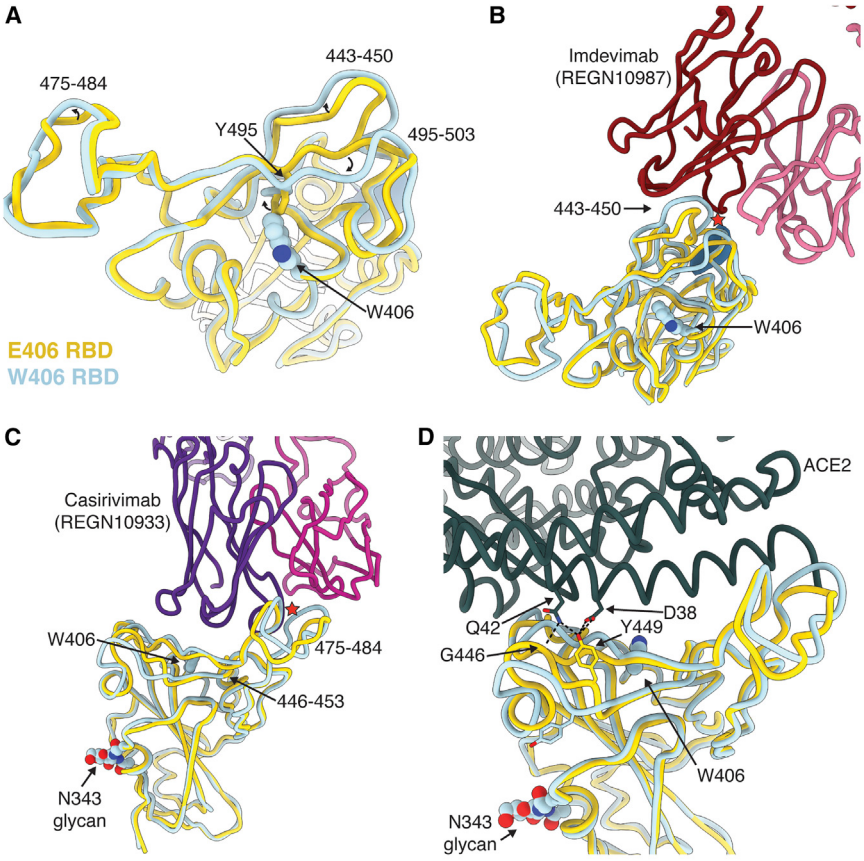

Figure 1. The E406W mutation remodels the SARS-CoV-2 RBD allosterically

(A), Structural superimposition of the Wuhan-Hu-1 RBD (E406, gold, PDB: 6M0J, ACE2 not displayed) and the W406 RBD (light blue).

(B and C) Structural superimposition of the REGN10987/REGN10933-bound Wuhan-Hu-1 RBD (E406, gold, PDB: 6XDG) and the W406 RBD (light blue). Steric clashes indicated with red stars.

(D) Structural superimposition of the ACE2-bound Wuhan-Hu-1 RBD (E406, gold, PDB: 6M0J) and the W406 RBD (light blue). Hydrogen bonds are shown as dotted lines.

an RBD reconstruction at 3.4 Å resolution, which was used for model building (enabling resolving the complete RBD) and analysis (Figures 1 and S1; Table S1).

The E406W substitution places the introduced side-chain indol ring in a position sterically incompatible with the neighboring Y495 phenol side chain, inducing a rotameric rearrangement of the latter residue relative to the ACE2-bound RBD structure[15] or apo S ectodomain trimer structures.[1,16] This results in major conformational reorganization of residues 443–450 and 495–503, which experience up to a 4.5 Å shift relative to previously determined structures[1,16] (the overall root-mean-square deviation [RMSD] between ACE2-bound RBD and E406W RBD is 1.37 Å over 194 C-alpha pairs). Although the organization of residues 475–484 is only subtly different in the E406W RBD relative to apo S structures,[1,16] it deviates more from the REGEN-COV-bound RBD structure[12] (Figures 1A and S2). REGN10987 recognizes an epitope residing at the interface between antigenic sites Ia and IIa[5] and forms extensive interactions with residues 440–449 that would sterically clash with the mAb heavy chain in the E406W RBD structure (Figure 1B). REGN10933 interacts with residues 417, 453–456, and 475–490 (within antigenic site Ia[5]), and the distinct conformation of the latter residues in the REGEN-COV-bound RBD and E406W apo S structures possibly precludes mAb binding through steric clash with the mAb light chain (Figure 1C). Our data therefore show that the E406W mutation disrupts the antigenic sites recognized by REGN10933 and REGN10987 allosterically, which are positioned 5 and 20 Å away, respectively.[10] Similar to REGN10987, the loss of COV2-2130 binding to the E406W RBD[14] is explained by the structural reorganization of residues 443–450, which are recognized by this mAb (Figure S3).

These RBD conformational changes also alter the ACE2-interacting surface, resulting in the predicted loss of several hydrogen bonds formed between the ACE2 D38 and SARS-CoV-2 Y449 side chains as well as the ACE2 Q42 side chain and the SARS-CoV-2 Y449 side chain and G446 main chain carbonyl (Figure 1D). Moreover, repositioning of residues 496–502 would likely also hinder ACE2 binding sterically. Accordingly, we observed that the monomeric human ACE2 ectodomain bound with a 14-fold reduced affinity to the immobilized SARS-CoV-2 E406W RBD (K_D = 1.34 μM) relative to the wild type (Wuhan-Hu-1) RBD (K_D = 93.9 nM) using biolayer interferometry (Figures 2A–2C; Table S2). This reduction of ACE2 binding affinity is expected to dampen viral fitness, as previously observed for another point mutation decreasing ACE2 binding[17] (Figure 2D) and for XBB.1 relative to XBB.1.5.[18]

Several broadly neutralizing sarbecovirus human mAbs recognizing distinct RBD antigenic sites have been described. Some of them were shown to be (partially) resilient to the ongoing SARS-CoV-2 evolution and to protect small animals against challenge with SARS-CoV-2 variants of concern or other sarbecoviruses.[11,17,20–26] To evaluate the influence of the aforementioned structural changes on neutralization by these mAbs, we compared the concentration-dependent inhibition of S309, S2E12, and S2X259 against vesicular stomatitis virus (VSV) particles pseudotyped with the Wuhan-Hu-1 spike harboring the G614 or the W406/G614 mutations. Each of these three mAbs neutralized with comparable potency the G614 and W406/G614 pseudoviruses (Table 1), indicating that they retain activity against this mutant (Figures 3A and S4). As predicted based on structural data,[5,11] the S2H14 mAb failed to neutralize the spike W406/G614 pseudovirus due to the reorganization of the RBM (Figures 2A and S5). Moreover, these data are consistent with

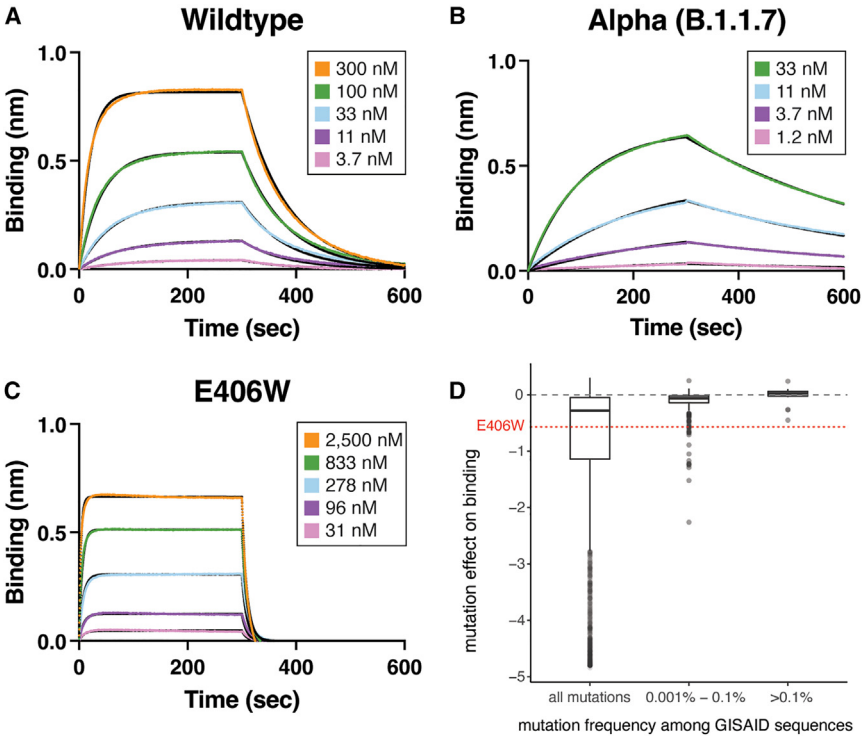

Figure 2. The E406W mutation dampens ACE2 binding severely

(A–C) Biolayer interferometry binding analysis of monomeric human ACE2 to immobilized Wuhan-Hu-1 (A), Alpha (N501Y, B), or E406W (C) RBDs.

(D) Mutation effects on avidity for dimeric human ACE2 as measured by yeast surface display[19] for the E406W mutation and RBD mutations found in human-derived SARS-CoV-2 isolates deposited in GISAID as of September 27, 2021, across increasing frequency thresholds.

the fact that binding to the SARS-CoV-2 E406W RBD was unaffected for S2E12 and abrogated for S2H14.[11]

Finally, we set out to assess the impact of the E406W mutation on vaccine-elicited plasma neutralizing activity using samples obtained from individuals who had received a primary vaccine series (2 doses) of either the Pfizer BNT162b2 or Moderna mRNA-1273 COVID-19 vaccine (Table S3). We observed 2.5- (BNT162b2, range: 1.2–4.6) and 2.4-fold (mRNA-1273, range: 1.5–3.8) reduction in neutralization potencies against the E406W/G614 spike pseudovirus compared with the G614 spike-harboring pseudovirus (Figures 3B, 3C, and S5). These data indicate that the single E406W mutation leads to moderate erosion of vaccine-elicited polyclonal neutralizing antibodies, comparable to the SARS-CoV-2 Epsilon variant[27] or the Delta variant.[28]

The ongoing SARS-CoV-2 evolution has yielded variants harboring numerous mutations, some of them altering transmissibility, immune evasion, replication kinetics, or disease severity relative to the ancestral SARS-CoV-2 strain.[7,27,29–44] We note that the E406W mutation requires multiple nucleotide substitutions from the Wuhan-Hu-1 spike sequence and has a deleterious effect on ACE2 binding. However, several currently circulating variants harbor amino acid mutations generated through multiple nucleotide substitutions (e.g., BA.1 S371L, BA.2.3.20 E484R, or XBB.1.5 G339H, V445P, and F486P) as well as mutations that dampen ACE2 binding in the Wuhan-Hu-1 background but are tolerated through epistatic interactions with other mutations (e.g., Q498R found in Omicron lineages).[45–47] This suggests that epistasis might allow for the future emergence of variants harboring the E406W mutation or other mutations remodeling RBD antigenic sites allosterically, especially as existing immunity drives selection of variants with enhanced capacity to evade neutralizing antibodies.[48] Furthermore, several emerging variants that were initially detected in wastewater are accumulating mutations in the antigenic sites affected by the E406W mutation,[49] underscoring its potential importance. The identification of the N501Y substitution, which enhances ACE2 binding, before its emergence in the Alpha variant and fixation in Omicron variants[19] highlights the power of deep-mutational scanning for prospective mapping of the effect of mutations to the SARS-CoV-2 RBD and motivates the characterization of unusual mutants, such as E406W. These results are reminiscent of the BA.2 and BA.4/5 S371F mutation, which dampens S309 binding via remodeling of the RBD helix comprising residues 364–372, which are outside the epitope of this mAb, likely by altering the N343 glycan conformation.[25] To conclude, our data showcase the structural and functional plasticity of the SARS-CoV-2 RBD,[19] suggesting that mutations influencing the organization of the RBD may accumulate and can be functionally tolerated within emerging SARS-CoV-2 strains.

Table 1. IC_{50} values for the four monoclonal antibodies tested against wild-type (G164) and E406W pseudoviruses

	IC_{50} against WT pseudovirus (ng/mL)	IC_{50} against E406W pseudovirus (ng/mL)
S309	26.6 ± 3.7	27.3 ± 2.4
S2E12	0.81 ± 0.19	0.98 ± 0.17
S2X259	39.4 ± 9.2	33.8 ± 15.6
S2H14	535 ± 224	>20,000

Values are presented as mean ± standard error. WT, wild type.

Limitations of the study

In this study, we introduced the E406W mutation into the Wuhan-Hu-1 spike protein and examined the impact of this mutation on the structure of the RBD and the efficacy of vaccine-elicited sera to neutralize E406W pseudovirus. As SARS-CoV-2 has continued to accumulate mutations across the spike protein, performing these analyses on variant spike proteins with the E406W mutation would provide greater insight into the

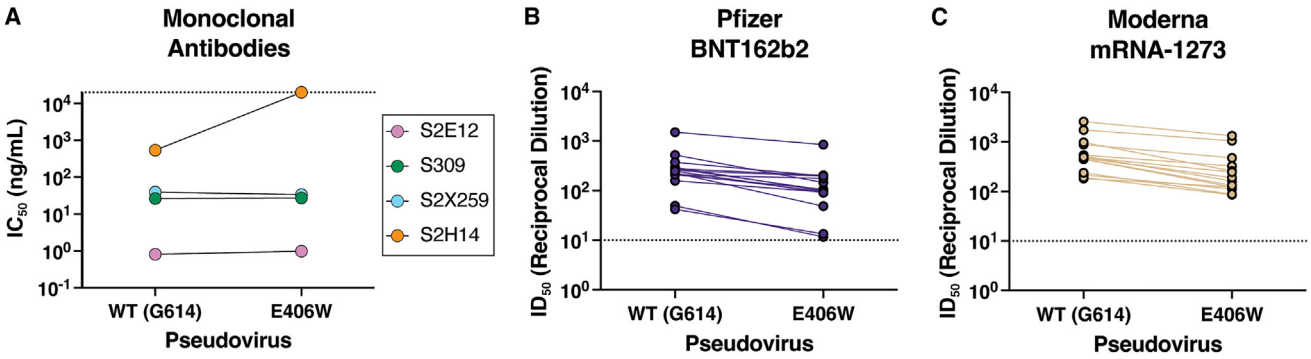

Figure 3. Evaluation of the neutralizing activity of several sarbecovirus broadly neutralizing mAbs and vaccine-elicited polyclonal antibodies

(A) Neutralization potency (50% inhibition concentration [IC_{50}]) of the mAbs S309, S2E12, S2X259, and S2H14 against VSV pseudotyped with either the wild-type (G614) or the E406W mutant spike protein. Non-neutralizing values are shown as 2×10^4 ng/mL, the limit of detection of the assay, as indicated by a dotted line. (B and C) Neutralization potency (50% inhibition dilution [ID_{50}]) of sera collected from individuals vaccinated with either Pfizer Cominarty (B) or Moderna's mRNA-1273 (C) against VSV pseudotyped with SARS-CoV-2 wild-type (G614) or E406W spike. ID_{50} values measured against the two pseudoviruses for each sample are connected by a line. The dotted line indicates the limit of detection of the assay.

plausibility of this mutation emerging in circulating variants. Furthermore, we used ACE2 binding and neutralization assays to estimate the fitness of a SARS-CoV-2 E406W viral variant compared with the Wuhan-Hu-1/G614 strain. Introducing this mutation into a replication-competent VSV-SARS-CoV-2-S system or equivalent may allow for a more complete understanding of the fitness cost of the E406W mutation.

STAR★METHODS

Detailed methods are provided in the online version of this paper and include the following:

- KEY RESOURCES TABLE
- RESOURCE AVAILABILITY
  - Lead contact
  - Materials availability
  - Data and code availability
- EXPERIMENTAL MODEL AND STUDY PARTICIPANT DETAILS
  - Cell culture
  - Sera
- METHOD DETAILS
  - Constructs
  - Recombinant protein expression and purification
  - Cryo-EM sample preparation and data collection
  - Cryo-EM data processing
  - Model building and refinement
  - Biolayer interferometry
  - Pseudotyped VSV production
  - Neutralization assays with vaccine-elicited sera and monoclonal antibodies
- QUANTIFICATION AND STATISTICAL ANALYSIS

SUPPLEMENTAL INFORMATION

Supplemental information can be found online at https://doi.org/10.1016/j.celrep.2023.112621.

ACKNOWLEDGMENTS

We thank Hideki Tani (University of Toyama) for providing the reagents necessary for preparing VSV pseudotyped viruses. This study was supported by the National Institute of Allergy and Infectious Diseases (DP1AI158186 and HHSN75N93022C00036 to D.V. and R01AI141707 to J.D.B.); the National Institute of General Medical Sciences (R01GM120553 to D.V.); the National Institute of Health Cellular and Molecular Biology Training Grant (T32GM007270 to A.A.); a Pew Biomedical Scholars Award (D.V.); an Investigators in the Pathogenesis of Infectious Disease Awards from the Burroughs Wellcome Fund (D.V. and J.D.B.); Fast Grants (D.V.); the Bill & Melinda Gates Foundation (OPP1156262 to D.V. and INV-004949 to J.D.B.); the University of Washington Arnold and Mabel Beckman cryo-EM center and the National Institutes of Health grant S10OD032290 (to D.V.); and grant U01 AI151698 for the United World Antiviral Research Network (UWARN) as part of the Centers for Research in Emerging Infectious Diseases (CREID) Network. T.S. is a Howard Hughes Medical Institute Fellow of the Damon Runyon Cancer Research Foundation. J.D.B. and D.V. are investigators of the Howard Hughes Medical Institute.

AUTHOR CONTRIBUTIONS

Conceptualization, A.A., T.S., A.J.G., J.E.B., A.C.W., and D.V.; pseudovirus entry assays, A.A. and A.C.W.; biolayer interferometry measurements, A.A.; provided unique reagents, D.C., S.W.T., and W.C.V.V.; data analysis, A.A. and D.V.; supervision, D.V.; writing – original draft, A.A. and D.V.; writing – review and editing, all authors.

DECLARATION OF INTERESTS

The Veesler laboratory has received a sponsored research agreement from Vir Biotechnology, Inc. J.D.B. consults for Moderna and Flagship Labs 77 on topics related to viral evolution and is an inventor on Fred Hutch licensed patents related to viral deep mutational scanning. D.C. is an employee of Vir Biotechnology, Inc., and may hold shares in Vir Biotechnology, Inc.

Received: November 9, 2022
Revised: April 18, 2023
Accepted: May 23, 2023
Published: May 26, 2023

REFERENCES

1. Walls, A.C., Park, Y.J., Tortorici, M.A., Wall, A., McGuire, A.T., and Veesler, D. (2020). Structure, function, and antigenicity of the SARS-CoV-2 spike glycoprotein. Cell *181*, 281–292.e6.

2. Zhou, P., Yang, X.L., Wang, X.G., Hu, B., Zhang, L., Zhang, W., Si, H.R., Zhu, Y., Li, B., Huang, C.L., et al. (2020). A pneumonia outbreak associated with a new coronavirus of probable bat origin. Nature *579*, 270–273. https://doi.org/10.1038/s41586-020-2012-7.

3. Hoffmann, M., Kleine-Weber, H., Schroeder, S., Krüger, N., Herrler, T., Erichsen, S., Schiergens, T.S., Herrler, G., Wu, N.H., Nitsche, A., et al. (2020). SARS-CoV-2 cell entry depends on ACE2 and TMPRSS2 and is blocked by a clinically proven protease inhibitor. Cell *181*, 271–280.e8.

4. Corti, D., Purcell, L.A., Snell, G., and Veesler, D. (2021). Tackling COVID-19 with neutralizing monoclonal antibodies. Cell *184*, 3086–3108. https://doi.org/10.1016/j.cell.2021.05.005.

5. Piccoli, L., Park, Y.J., Tortorici, M.A., Czudnochowski, N., Walls, A.C., Beltramello, M., Silacci-Fregni, C., Pinto, D., Rosen, L.E., Bowen, J.E., et al. (2020). Mapping neutralizing and immunodominant sites on the SARS-CoV-2 spike receptor-binding domain by structure-guided high-resolution serology. Cell *183*, 1024–1042.e21.

6. Greaney, A.J., Loes, A.N., Gentles, L.E., Crawford, K.H.D., Starr, T.N., Malone, K.D., Chu, H.Y., and Bloom, J.D. (2021). Antibodies elicited by mRNA-1273 vaccination bind more broadly to the receptor binding domain than do those from SARS-CoV-2 infection. Sci. Transl. Med. *13*, eabi9915. https://doi.org/10.1126/scitranslmed.abi9915.

7. McCallum, M., De Marco, A., Lempp, F.A., Tortorici, M.A., Pinto, D., Walls, A.C., Beltramello, M., Chen, A., Liu, Z., Zatta, F., et al. (2021). N-terminal domain antigenic mapping reveals a site of vulnerability for SARS-CoV-2. Cell *184*, 2332–2347.e16. https://doi.org/10.1016/j.cell.2021.03.028.

8. Stamatatos, L., Czartoski, J., Wan, Y.-H., Homad, L.J., Rubin, V., Glantz, H., Neradilek, M., Seydoux, E., Jennewein, M.F., MacCamy, A.J., et al. (2021). mRNA vaccination boosts cross-variant neutralizing antibodies elicited by SARS-CoV-2 infection. Science *372*, 1413–1418. https://doi.org/10.1126/science.abg9175.

9. Bowen, J.E., Walls, A.C., Joshi, A., Sprouse, K.R., Stewart, C., Tortorici, M.A., Franko, N.M., Logue, J.K., Mazzitelli, I.G., Tiles, S.W., et al. (2021). SARS-CoV-2 spike conformation determines plasma neutralizing activity. Preprint at bioRxiv. https://doi.org/10.1101/2021.12.19.473391.

10. Starr, T.N., Greaney, A.J., Addetia, A., Hannon, W.W., Choudhary, M.C., Dingens, A.S., Li, J.Z., and Bloom, J.D. (2021). Prospective mapping of viral mutations that escape antibodies used to treat COVID-19. Science *371*, 850–854.

11. Starr, T.N., Czudnochowski, N., Liu, Z., Zatta, F., Park, Y.-J., Addetia, A., Pinto, D., Beltramello, M., Hernandez, P., Greaney, A.J., et al. (2021). SARS-CoV-2 RBD antibodies that maximize breadth and resistance to escape. Nature *597*, 97–102. https://doi.org/10.1038/s41586-021-03807-6.

12. Hansen, J., Baum, A., Pascal, K.E., Russo, V., Giordano, S., Wloga, E., Fulton, B.O., Yan, Y., Koon, K., Patel, K., et al. (2020). Studies in humanized mice and convalescent humans yield a SARS-CoV-2 antibody cocktail. Science *369*, 1010–1014. https://doi.org/10.1126/science.abd0827.

13. Baum, A., Fulton, B.O., Wloga, E., Copin, R., Pascal, K.E., Russo, V., Giordano, S., Lanza, K., Negron, N., Ni, M., et al. (2020). Antibody cocktail to SARS-CoV-2 spike protein prevents rapid mutational escape seen with individual antibodies. Science *369*, 1014–1018. https://doi.org/10.1126/science.abd0831.

14. Dong, J., Zost, S.J., Greaney, A.J., Starr, T.N., Dingens, A.S., Chen, E.C., Chen, R.E., Case, J.B., Sutton, R.E., Gilchuk, P., et al. (2021). Genetic and structural basis for SARS-CoV-2 variant neutralization by a two-antibody cocktail. Nat. Microbiol. *6*, 1233–1244.

15. Lan, J., Ge, J., Yu, J., Shan, S., Zhou, H., Fan, S., Zhang, Q., Shi, X., Wang, Q., Zhang, L., and Wang, X. (2020). Structure of the SARS-CoV-2 spike receptor-binding domain bound to the ACE2 receptor. Nature *581*, 215–220. https://doi.org/10.1038/s41586-020-2180-5.

16. Wrobel, A.G., Benton, D.J., Xu, P., Roustan, C., Martin, S.R., Rosenthal, P.B., Skehel, J.J., and Gamblin, S.J. (2020). SARS-CoV-2 and bat RaTG13 spike glycoprotein structures inform on virus evolution and furin-cleavage effects. Nat. Struct. Mol. Biol. *27*, 763–767.

17. Park, Y.-J., De Marco, A., Starr, T.N., Liu, Z., Pinto, D., Walls, A.C., Zatta, F., Zepeda, S.K., Bowen, J.E., Sprouse, K.R., et al. (2022). Antibody-mediated broad sarbecovirus neutralization through ACE2 molecular mimicry. Science *375*, 449–454.

18. Yue, C., Song, W., Wang, L., Jian, F., Chen, X., Gao, F., Shen, Z., Wang, Y., Wang, X., and Cao, Y. (2023). ACE2 binding and antibody evasion in enhanced transmissibility of XBB.1.5. Lancet Infect. Dis. *23*, 278–280. https://doi.org/10.1016/S1473-3099(23)00010-5.

19. Starr, T.N., Greaney, A.J., Hilton, S.K., Ellis, D., Crawford, K.H.D., Dingens, A.S., Navarro, M.J., Bowen, J.E., Tortorici, M.A., Walls, A.C., et al. (2020). Deep mutational scanning of SARS-CoV-2 receptor binding domain reveals constraints on folding and ACE2 binding. Cell *182*, 1295–1310.e20.

20. Tortorici, M.A., Czudnochowski, N., Starr, T.N., Marzi, R., Walls, A.C., Zatta, F., Bowen, J.E., Jaconi, S., Di Iulio, J., Wang, Z., et al. (2021). Broad sarbecovirus neutralization by a human monoclonal antibody. Nature *597*, 103–108. https://doi.org/10.1038/s41586-021-03817-4.

21. Pinto, D., Park, Y.J., Beltramello, M., Walls, A.C., Tortorici, M.A., Bianchi, S., Jaconi, S., Culap, K., Zatta, F., De Marco, A., et al. (2020). Cross-neutralization of SARS-CoV-2 by a human monoclonal SARS-CoV antibody. Nature *583*, 290–295.

22. Tortorici, M.A., Beltramello, M., Lempp, F.A., Pinto, D., Dang, H.V., Rosen, L.E., McCallum, M., Bowen, J., Minola, A., Jaconi, S., et al. (2020). Ultrapotent human antibodies protect against SARS-CoV-2 challenge via multiple mechanisms. Science *370*, 950–957.

23. Jette, C.A., Cohen, A.A., Gnanapragasam, P.N.P., Muecksch, F., Lee, Y.E., Huey-Tubman, K.E., Schmidt, F., Hatziioannou, T., Bieniasz, P.D., Nussenzweig, M.C., et al. (2021). Broad cross-reactivity across sarbecoviruses exhibited by a subset of COVID-19 donor-derived neutralizing antibodies. Cell Rep. *37*, 110188.

24. Martinez, D.R., Schäfer, A., Gobeil, S., Li, D., De la Cruz, G., Parks, R., Lu, X., Barr, M., Stalls, V., Janowska, K., et al. (2022). A broadly cross-reactive antibody neutralizes and protects against sarbecovirus challenge in mice. Sci. Transl. Med. *14*, eabj7125.

25. Park, Y.-J., Pinto, D., Walls, A.C., Liu, Z., De Marco, A., Benigni, F., Zatta, F., Silacci-Fregni, C., Bassi, J., Sprouse, K.R., et al. (2022). Imprinted antibody responses against SARS-CoV-2 Omicron sublineages. Science *378*, 619–627.

26. Westendorf, K., Žentelis, S., Wang, L., Foster, D., Vaillancourt, P., Wiggin, M., Lovett, E., van der Lee, R., Hendle, J., Pustilnik, A., et al. (2022). LY-CoV1404 (bebtelovimab) potently neutralizes SARS-CoV-2 variants. Cell Rep. *39*, 110812.

27. McCallum, M., Bassi, J., De Marco, A., Chen, A., Walls, A.C., Di Iulio, J., Tortorici, M.A., Navarro, M.-J., Silacci-Fregni, C., Saliba, C., et al. (2021). SARS-CoV-2 immune evasion by the B.1.427/B.1.429 variant of concern. Science *373*, 648–654. https://doi.org/10.1126/science.abi7994.

28. McCallum, M., Walls, A.C., Sprouse, K.R., Bowen, J.E., Rosen, L.E., Dang, H.V., De Marco, A., Franko, N., Tilles, S.W., Logue, J., et al. (2021). Molecular basis of immune evasion by the Delta and Kappa SARS-CoV-2 variants. Science *374*, 1621–1626.

29. Davies, N.G., Abbott, S., Barnard, R.C., Jarvis, C.I., Kucharski, A.J., Munday, J.D., Pearson, C.A.B., Russell, T.W., Tully, D.C., Washburne, A.D., et al. (2021). Estimated transmissibility and impact of SARS-CoV-2 lineage B.1.1.7 in England. Science. https://doi.org/10.1126/science.abg3055.

30. Tegally, H., Wilkinson, E., Giovanetti, M., Iranzadeh, A., Fonseca, V., Giandhari, J., Doolabh, D., Pillay, S., San, E.J., Msomi, N., et al. (2021). Emergence of a SARS-CoV-2 variant of concern with mutations in spike

glycoprotein. Nature *592*, 438–443. https://doi.org/10.1038/s41586-021-03402-9.

31. Deng, X., Garcia-Knight, M.A., Khalid, M.M., Servellita, V., Wang, C., Morris, M.K., Sotomayor-González, A., Glasner, D.R., Reyes, K.R., Gliwa, A.S., et al. (2021). Transmission, infectivity, and neutralization of a spike L452R SARS-CoV-2 variant. Cell *184*, 3426–3437.e8. https://doi.org/10.1016/j.cell.2021.04.025.
32. Faria, N.R., Mellan, T.A., Whittaker, C., Claro, I.M., Candido, D.d.S., Mishra, S., Crispim, M.A.E., Sales, F.C.S., Hawryluk, I., McCrone, J.T., et al. (2021). Genomics and epidemiology of the P.1 SARS-CoV-2 lineage in Manaus, Brazil. Science *372*, 815–821.
33. Thomson, E.C., Rosen, L.E., Shepherd, J.G., Spreafico, R., da Silva Filipe, A., Wojcechowskyj, J.A., Davis, C., Piccoli, L., Pascall, D.J., Dillen, J., et al. (2021). Circulating SARS-CoV-2 spike N439K variants maintain fitness while evading antibody-mediated immunity. Cell *184*, 1171–1187.e20. https://doi.org/10.1016/j.cell.2021.01.037.
34. Collier, D.A., De Marco, A., Ferreira, I.A.T., Meng, B., Datir, R.P., Walls, A.C., Kemp, S.A., Bassi, J., Pinto, D., Silacci-Fregni, C., et al. (2021). Sensitivity of SARS-CoV-2 B.1.1.7 to mRNA vaccine-elicited antibodies. Nature *593*, 136–141. https://doi.org/10.1038/s41586-021-03412-7.
35. Cele, S., Gazy, I., Jackson, L., Hwa, S.-H., Tegally, H., Lustig, G., Giandhari, J., Pillay, S., Wilkinson, E., Naidoo, Y., et al. (2021). Escape of SARS-CoV-2 501Y.V2 from neutralization by convalescent plasma. Nature *593*, 142–146. https://doi.org/10.1038/s41586-021-03471-w.
36. Wibmer, C.K., Ayres, F., Hermanus, T., Madzivhandila, M., Kgagudi, P., Oosthuysen, B., Lambson, B.E., de Oliveira, T., Vermeulen, M., van der Berg, K., et al. (2021). SARS-CoV-2 501Y.V2 escapes neutralization by South African COVID-19 donor plasma. Nat. Med. *27*, 622–625. https://doi.org/10.1038/s41591-021-01285-x.
37. Edara, V.-V., Pinsky, B.A., Suthar, M.S., Lai, L., Davis-Gardner, M.E., Floyd, K., Flowers, M.W., Wrammert, J., Hussaini, L., Ciric, C.R., et al. (2021). Infection and vaccine-induced neutralizing-antibody responses to the SARS-CoV-2 B.1.617 variants. N. Engl. J. Med. *385*, 664–666. https://doi.org/10.1056/NEJMc2107799.
38. Liu, C., Ginn, H.M., Dejnirattisai, W., Supasa, P., Wang, B., Tuekprakhon, A., Nutalai, R., Zhou, D., Mentzer, A.J., Zhao, Y., et al. (2021). Reduced neutralization of SARS-CoV-2 B.1.617 by vaccine and convalescent serum. Cell *184*, 4220–4236.e13. https://doi.org/10.1016/j.cell.2021.06.020.
39. Plante, J.A., Liu, Y., Liu, J., Xia, H., Johnson, B.A., Lokugamage, K.G., Zhang, X., Muruato, A.E., Zou, J., Fontes-Garfias, C.R., et al. (2021). Spike mutation D614G alters SARS-CoV-2 fitness. Nature *592*, 116–121. https://doi.org/10.1038/s41586-020-2895-3.
40. Liu, Y., Liu, J., Johnson, B.A., Xia, H., Ku, Z., Schindewolf, C., Widen, S.G., An, Z., Weaver, S.C., Menachery, V.D., et al. (2021). Delta spike P681R mutation enhances SARS-CoV-2 fitness over Alpha variant. Preprint at bioRxiv. https://doi.org/10.1101/2021.08.12.456173.
41. Saito, A., Irie, T., Suzuki, R., Maemura, T., Nasser, H., Uriu, K., Kosugi, Y., Shirakawa, K., Sadamasu, K., Kimura, I., et al. (2022). Enhanced fusogenicity and pathogenicity of SARS-CoV-2 Delta P681R mutation. Nature *602*, 300–306. https://doi.org/10.1038/s41586-021-04266-9.
42. Cameroni, E., Bowen, J.E., Rosen, L.E., Saliba, C., Zepeda, S.K., Culap, K., Pinto, D., VanBlargan, L.A., De Marco, A., di Iulio, J., et al. (2022). Broadly neutralizing antibodies overcome SARS-CoV-2 Omicron antigenic shift. Nature *602*, 664–670.
43. McCallum, M., Czudnochowski, N., Rosen, L.E., Zepeda, S.K., Bowen, J.E., Walls, A.C., Hauser, K., Joshi, A., Stewart, C., Dillen, J.R., et al. (2022). Structural basis of SARS-CoV-2 Omicron immune evasion and receptor engagement. Science *375*, 864–868.
44. Meng, B., Abdullahi, A., Ferreira, I.A.T., Goonawardane, N., Saito, A., Kimura, I., Yamasoba, D., Gerber, P.P., Fatihi, S., Rathore, S., et al. (2022). Altered TMPRSS2 usage by SARS-CoV-2 Omicron impacts infectivity and fusogenicity. Nature *603*, 706–714.
45. Starr, T.N., Greaney, A.J., Hannon, W.W., Loes, A.N., Hauser, K., Dillen, J.R., Ferri, E., Farrell, A.G., Dadonaite, B., McCallum, M., et al. (2022). Shifting mutational constraints in the SARS-CoV-2 receptor-binding domain during viral evolution. Preprint at bioRxiv. *377*, 420–424. https://doi.org/10.1101/2022.02.24.481899.
46. Viana, R., Moyo, S., Amoako, D.G., Tegally, H., Scheepers, C., Althaus, C.L., Anyaneji, U.J., Bester, P.A., Boni, M.F., Chand, M., et al. (2022). Rapid epidemic expansion of the SARS-CoV-2 Omicron variant in southern Africa. Nature *603*, 679–686.
47. Dejnirattisai, W., Huo, J., Zhou, D., Zahradník, J., Supasa, P., Liu, C., Duyvesteyn, H.M.E., Ginn, H.M., Mentzer, A.J., Tuekprakhon, A., et al. (2022). SARS-CoV-2 Omicron-B.1.1.529 leads to widespread escape from neutralizing antibody responses. Cell *185*, 467–484.e15.
48. Greaney, A.J., Starr, T.N., Eguia, R.T., Loes, A.N., Khan, K., Karim, F., Cele, S., Bowen, J.E., Logue, J.K., Corti, D., et al. (2022). A SARS-CoV-2 variant elicits an antibody response with a shifted immunodominance hierarchy. PLoS Pathog. *18*, e1010248.
49. Gregory, D.A., Trujillo, M., Rushford, C., Flury, A., Kannoly, S., San, K.M., Lyfoung, D.T., Wiseman, R.W., Bromert, K., Zhou, M.-Y., et al. (2022). Genetic diversity and evolutionary convergence of cryptic SARS- CoV-2 lineages detected via wastewater sequencing. PLoS Pathog. *18*, e1010636. https://doi.org/10.1371/journal.ppat.1010636.
50. Crawford, K.H.D., Eguia, R., Dingens, A.S., Loes, A.N., Malone, K.D., Wolf, C.R., Chu, H.Y., Tortorici, M.A., Veesler, D., Murphy, M., et al. (2020). Protocol and reagents for pseudotyping lentiviral particles with SARS-CoV-2 spike protein for neutralization assays. Viruses *12*. https://doi.org/10.3390/v12050513.
51. Hsieh, C.-L., Goldsmith, J.A., Schaub, J.M., DiVenere, A.M., Kuo, H.-C., Javanmardi, K., Le, K.C., Wrapp, D., Lee, A.G., Liu, Y., et al. (2020). Structure-based design of prefusion-stabilized SARS-CoV-2 spikes. Science *369*, 1501–1505.
52. Russo, C.J., and Passmore, L.A. (2014). Electron microscopy: ultrastable gold substrates for electron cryomicroscopy. Science *346*, 1377–1380.
53. Suloway, C., Pulokas, J., Fellmann, D., Cheng, A., Guerra, F., Quispe, J., Stagg, S., Potter, C.S., and Carragher, B. (2005). Automated molecular microscopy: the new Leginon system. J. Struct. Biol. *151*, 41–60.
54. Tegunov, D., and Cramer, P. (2019). Real-time cryo-electron microscopy data preprocessing with Warp. Nat. Methods *16*, 1146–1152.
55. Punjani, A., Rubinstein, J.L., Fleet, D.J., and Brubaker, M.A. (2017). cryoSPARC: algorithms for rapid unsupervised cryo-EM structure determination. Nat. Methods *14*, 290–296.
56. Punjani, A., Zhang, H., and Fleet, D.J. (2020). Non-uniform refinement: adaptive regularization improves single-particle cryo-EM reconstruction. Nat. Methods *17*, 1214–1221.
57. Zivanov, J., Nakane, T., and Scheres, S.H.W. (2019). A Bayesian approach to beam-induced motion correction in cryo-EM single-particle analysis. IUCrJ *6*, 5–17.
58. Zivanov, J., Nakane, T., Forsberg, B.O., Kimanius, D., Hagen, W.J., Lindahl, E., and Scheres, S.H. (2018). New tools for automated high-resolution cryo-EM structure determination in RELION-3. Elife *7*. https://doi.org/10.7554/eLife.42166.
59. Scheres, S.H.W. (2012). RELION: implementation of a Bayesian approach to cryo-EM structure determination. J. Struct. Biol. *180*, 519–530.
60. Rosenthal, P.B., and Henderson, R. (2003). Optimal determination of particle orientation, absolute hand, and contrast loss in single-particle electron cryomicroscopy. J. Mol. Biol. *333*, 721–745.
61. Chen, S., McMullan, G., Faruqi, A.R., Murshudov, G.N., Short, J.M., Scheres, S.H.W., and Henderson, R. (2013). High-resolution noise substitution to measure overfitting and validate resolution in 3D structure determination by single particle electron cryomicroscopy. Ultramicroscopy *135*, 24–35.

62. Pettersen, E.F., Goddard, T.D., Huang, C.C., Couch, G.S., Greenblatt, D.M., Meng, E.C., and Ferrin, T.E. (2004). UCSF Chimera–a visualization system for exploratory research and analysis. J. Comput. Chem. *25*, 1605–1612.

63. Emsley, P., Lohkamp, B., Scott, W.G., and Cowtan, K. (2010). Features and development of Coot. Acta Crystallogr. D Biol. Crystallogr. *66*, 486–501.

64. Frenz, B., Rämisch, S., Borst, A.J., Walls, A.C., Adolf-Bryfogle, J., Schief, W.R., Veesler, D., and DiMaio, F. (2019). Automatically fixing errors in glycoprotein structures with Rosetta. Structure *27*, 134–139.e3.

65. Wang, R.Y.-R., Song, Y., Barad, B.A., Cheng, Y., Fraser, J.S., and DiMaio, F. (2016). Automated structure refinement of macromolecular assemblies from cryo-EM maps using Rosetta. Elife *5*, e17219. https://doi.org/10.7554/eLife.17219.

STAR★METHODS

KEY RESOURCES TABLE

REAGENT or RESOURCE	SOURCE	IDENTIFIER
Antibodies		
S309	Pinto et al.; 2020	N/A
S2H14	Piccoli et al.; 2020	N/A
S2X259	Tortorici et al.; 2021	N/A
S2E12	Tortorici et al.; 2020	N/A
Bacterial and virus strains		
VSV (G*ΔG-luciferase)	Kaname et al., 2010	N/A
Biological samples		
SARS-CoV-2 vaccinated human sera and plasma	UWARN: COVID-19 in WA study at the University of Washington	N/A
Chemicals, peptides, and recombinant proteins		
ONE-Glo EX	Promega	Cat#E8110
Expifectamine 293	Thermo Fisher	Cat#A14524
Lipofectamine 2000	Thermo Fisher	Cat#11668019
BirA biotin-protein ligase	Avidity	Cat#BirA500
PEI MAX	Polysciences	Cat#24765
Deposited data		
SARS-CoV-2 S E406W cryoEM maps	This paper.	EMDB: EMD-26056 (Ectodomain); EMDB: EMD-26058 (RBD)
SARS-CoV-2 S E406W atomic models	This paper.	PDB: 7TPI (Ectodomain); PDB: 7TPK (RBD)
Experimental models: Cell lines		
Expi293F	Thermo Fisher	Cat#A14635
HEK293T/17	ATCC	Cat#CRL-11268
HEK293-hACE2	BEI; Crawford et al., 2020	N/A
VeroE6-TMPRSS2	Lempp et al., 2021	N/A
I1-Hybridoma	ATCC	Cat#CRL-2700
Recombinant DNA		
SARS-CoV-2 S ectodomain E406W	UW Institute for Protein Design	N/A
SARS-CoV-2 RBD wildtype	Genscript + subcloning; Walls et al.; 2020	N/A
SARS-CoV-2 RBD Alpha (B.1.1.7)	Genscript + subcloning; Collier et al.; 2021	N/A
SARS-COV-2 RBD E406W	Genscript + subcloning	N/A
SARS-CoV-2 full length S del 21 D614G	BEI; Crawford et al., 2020	Cat#BEI NR-52514
SARS-CoV-2 full length S del 21 E406W	Genscript + subcloning	N/A
Human ACE2 ectodomain	Twist Bioscience	N/A
Software and algorithms		
Prism	GraphPad	https://www.graphpad.com/
Octet Data Analysis HT software	Sartorius	https://www.sartorius.com/en/products/protein-analysis/octet-bli-detection/octet-systems-software
Leginon	Suloway et al., 2005	http://emg.nysbc.org/redmine/projects/leginon/wiki/Leginon_Homepage
WARP	Tegunov and Cramer, 2019	https://github.com/cramerlab/warp
cryoSPARC	Punjani et al., 2017	https://cryosparc.com

(*Continued on next page*)

Continued

REAGENT or RESOURCE	SOURCE	IDENTIFIER
Relion	Scheres and Chen, 2012; Zivanov et al., 2019	=https://www2.mrc-lmb.cam.ac.uk/relion/index.php?title=MainPage
UCSF Chimera	Goddard et al., 2007	https://www.rbvi.ucsf.edu/chimera/
Coot	Emsley et al., 2010	https://www2.mrc-lmb.cam.ac.uk/personal/pemsley/coot/
Rosetta	Frenz et al., 2019; Wang et al., 2016	https://www.rosettacommons.org/software
UCSF ChimeraX	Goddard et al., 2018	https://www.rbvi.ucsf.edu/chimerax/
Other		
2.0/2.0 UltraFoil grid (200 mesh)	Electron Microscopy Sciences	Cat#Q250AR2A
HisTrap FF	Cytiva	Cat#17531901
HisTrap HP	Cytiva	Cat#29051021
Octet Streptavidin (SA) Biosensors	Sartorius	Cat#18-5019

RESOURCE AVAILABILITY

Lead contact

Correspondence and requests for materials should be addressed to David Veesler (dveesler@uw.edu).

Materials availability

Plasmids generated in this study will be available upon request with a completed Materials Transfer Agreement.

Data and code availability

- Cryo-EM maps and atomic models have been deposited at the Electron Microscopy DataBank and the Protein DataBank under the following accession codes: EMD: EMD-26058 and PDB: 7TPK (SARS-CoV-2 E406W RBD) and EMD: EMD-26056 and PDB: 7TPI (SARS-CoV-2 E406W Ectodomain).
- This paper does not report original code.
- Any additional information required to reanalyze the data reported in this paper is available from the lead contact upon request.

EXPERIMENTAL MODEL AND STUDY PARTICIPANT DETAILS

Cell culture

Expi293 cells were grown in Expi293 media at 37°C and 8% CO_2 rotating at 130 RPM. HEK-293T cells and HEK-293T cells stably expressing the human ACE2 receptor (HEK-ACE2)[50] were grown in DMEM supplemented with 10% FBS and 1% PenStrep at 37°C and 5% CO_2. Vero cells stably expressing the human protease TMPRSS2 (Vero-TMPRSS2) were grown in DMEM supplemented with 10% FBS, 1% PenStrep, and 8 μg/mL puromycin at 37°C and 5% CO_2.

Sera

Blood samples were collected from individuals 7–30 days after receiving the second dose of either Pfizer's BNT162b2 or Moderna's mRNA-1273 COVID-19 vaccine. All study participants were enrolled in the UWARN: COVID-19 in WA study at the University of Washington. The study protocol was approved by the University of Washington Human Subjects Division Institutional Review Board (STUDY00010350). Demographic information, including age and sex, for sera donors is provided in Table S3.

METHOD DETAILS

Constructs

The construct encoding spike ectodomain harboring the E406W mutation was obtained from the Institute for Protein Design. The spike ectodomain was codon optimized, stabilized with the hexapro mutations[51] and mutation of the furin cleavage site ($_{682}$RRAR$_{685}$ to $_{682}$GSAS$_{685}$), and inserted into the pCDNA3.1 vector containing a C-terminal foldon followed by an avi tag and an octa-histidine tag.

The construct encoding the E406W RBD was generated by performing around-the-horn mutagenesis using a pCMVR vector encoding the wildtype SARS-CoV-2 RBD containing an N-terminal mu-phosphatase signal peptide and a C-terminal avi tag and octa-histidine tag. The boundaries for the SARS-CoV-2 RBD in this construct were $_{328}$RFPN$_{331}$ to $_{528}$KKST$_{531}$.

Recombinant protein expression and purification

To produce the SARS-CoV-2 spike ectodomain containing the E406W mutation, 125 mL of Expi293 cells were grown to density of 2.5 x 10^6 cells per mL and transfected with 125 μg of DNA using PEI MAX diluted in Opti-MEM. The cells were grown for four days after which the supernatant was clarified by centrifugation. The recombinant ectodomain was purified using a nickel HisTrap FF affinity column, washed with 10 column volumes of 20 mM imidazole, 25 mM sodium phosphate pH 8.0, and 300 mM NaCl, and eluted with a 500 mM imidazole gradient. The purified proteins were buffer exchanged and concentrated in 20 mM sodium phosphate pH 8 and 100 mM NaCl using a 100 kDa centrifugal filter. The proteins were flash frozen and stored at −80°C until use.

The wildtype, B.1.1.7, and E406W RBDs were produced by transfecting 25 mL of Expi293 cells at a density of 2.5 x 10^6 cells per mL with 25 μg of DNA using the ExpiFectamine 293 Transfection Kit. The cells were grown for four days and the resulting supernatant was collected and clarified by centrifugation. The recombinant RBD was purified using a nickel HisTrap HP affinity column, washed with 10 column volumes of 20 mM imidazole, 25 mM sodium phosphate pH 8.0, and 300 mM NaCl, and eluted using a 500 mM imidazole gradient. The resulting protein was buffer exchanged and concentrated using a 10 kDa centrifugal filter. Next, the purified RBDs were biotinylated using the BirA biotin-protein ligase reaction kit (Avidity). The biotinylated proteins were re-purified and concentrated as described above. The proteins were flash frozen and stored at −80°C until use.

Cryo-EM sample preparation and data collection

3 μL of purified SARS-CoV-2 spike ectodomain harboring the E406W mutation at a concentration of 1.6 mg/mL was added to a freshly glow discharged 2.0/2.0 UltraFoil grid[52] (200 mesh). The grid was then plunge frozen using a Vitrobot MarkIV (ThermoFisher) with a blotting force of 0 and time of 6.5 s at 100% humidity and 23°C. Data were acquired on a FEI Titan Krios transmission electron microscope operated at 300 kV and equipped with a Gatan K3 direct detector and Gatan Quantum GIF energy filter, operated in zero-loss mode with a slit width of 20 eV. Automated data acquisition was carried out using Leginon.[53] The dose rate was adjusted to 15 counts/pixel/s and each movie was acquired in 75 frames of 40 ms with pixel size of 0.843 Å and a defocus range comprised between −0.1 and −2.6 μm.

Cryo-EM data processing

Movie frame alignment, estimation of the microscope CTF, particle picking, and extraction (with a downsampled pixel size of 1.686 Å and box size of 260 pixels^2) were completed using WARP.[54] Reference-free 2D classification was performed using cryoSPARC to select for well-defined particle images.[55] These selected particles were then used for 3D classification with 50 iterations (angular sampling 7.5° for 25 iterations followed by 1.8° with local search for 25 iterations) using Relion and a previously reported closed model for the SARS-CoV-2 spike ectodomain (PBD: 6VXX) as the initial model without imposing any symmetry. 3D refinements were carried out using non-uniform refinement along with per-particle defocus refinement in cryoSPARC[56] after which particles images were subjected to Bayesian polishing using Relion[57] and re-extracted with a box size of 512 pixels and a pixel size of 1 Å. Another round of non-uniform refinement followed by per-particle defocus refinement followed by another non-uniform refinement was conducted in cryoSPARC. Next, 86 optics groups were defined based on the beamtilt angle used for data collection and another round of non-uniform refinement with global and per-particle defocus refinement concurrently was conducted in cryoSPARC. To better resolve the RBD, focus 3D classification was carried out using symmetry expanded particles and a mask over residues 440–452 and 495–505 of the RBD using a tau factor of 200 in Relion.[58,59] Particles from the classes with the best resolved local density were selected and then subjected to local refinement using cryoSPARC. Reported resolutions are based on the gold-standard Fourier shell correlation of 0.143 criterion and Fourier shell correlation curves were corrected for the effects of soft masking by high-resolution noise substitution.[60,61]

Model building and refinement

USCF Chimera[62] and Coot[63] were used to fit atomic models of the SARS-CoV-2 RBD and ectodomain (PBD: 6M0J, 7LXY). Models were refined and rebuilt into the map using Coot[63] and Rosetta[64,65] with the RBD model being built using the map obtained from local refinement of the RBD and the ectodomain model being built using the map obtained for the three-fold symmetric ectodomain.

Biolayer interferometry

Biotinylated wildtype, B.1.1.7, or E406W RBD at a concentration of 5 ng/μL in 10X kinetics buffer was loaded at 30C onto pre-hydrated streptavidin biosensor to a 1 nm total shift. The loaded tips were then dipped into a 1:3 dilution series of monomeric hACE2 beginning at 900 nM, 300 nM, or 7,500 nM for 300 s followed by dissociation in 10X kinetics buffer for 300 s. The resulting data were baseline subtracted and curves were fitted using Octet Data Analysis HT software v12.0 and plotted in GraphPad Prism 9.

Pseudotyped VSV production

E406W and wildtype pseudotyped VSV particles were produced as previously described.[27,28] Briefly, 5 x 10^6 HEK-293T cells were seeded in 10 cm^2 poly-D-lysine coated plates and grown overnight until they reached ~70% confluency. The cells were then washed 5 times with Opti-MEM (Life Technologies) and transfected with 24 μg of plasmid encoding either the wildtype or E406W SARS-CoV-2 spike protein using Lipofectamine 2000 (Life Technologies). Four hours at transfection, an equal volume of DMEM supplemented with 20% FBS and 2% PenStrep was added to the cells. Twenty to 24 h following transfection, the cells were washed 5 times with

DMEM and infected with VSVΔG/Fluc. Two hours after infection, the cells were washed 5 times with DMEM and grown in DMEM supplemented with 10% FBS and 1% PenStrep along with an anti-VSV-G antibody (I1-mouse hybridoma supernatant diluted 1:25, from CRL-2700, ATCC). Twenty to 24 h later, the supernatant was collected, clarified by centrifugation at 2,500xg for 10 min, filtered through a 0.45 μm filter, and concentrated 10x using a 30 kDa filter (Amicon). The resulting pseudovirus was frozen at −80°C until use.

Neutralization assays with vaccine-elicited sera and monoclonal antibodies

For neutralization assays using vaccine-elicited sera, HEK-ACE2 cells were seeded in 96-well poly-D-lysine coated plates at a density of 30,000 cells per well and grown overnight until they reached approximately 80% confluency. E406W and wildtype pseudoviruses were diluted 1:25 in DMEM and incubated with vaccine-elicited sera for 30 min at room temperature. Growth media was removed from the HEK-ACE2 cells and the virus-sera mixture was added to the cells. Two hours after infection, an equal volume of DMEM supplemented with 20% and 2% PenStrep was added to each well and the cells were incubated overnight. After 20–24 h, ONE-Glo EX (Promega) was added to each well and the cells were incubated for 5 min at 37°C. Luminescence values were measured using a BioTek plate reader.

For neutralization assays using monoclonal antibodies, Vero-TMPRSS2 cells were seeded in 96-well plates at a density of 18,000 cells per overnight until they reached approximately 80% confluency. Neutralizations were conducted as described above with one modification: prior to the addition of the virus-antibody mixture, Vero-TMPRSS2 cells were washed 3 times with DMEM.

Luminescence readings from the neutralization assays were normalized and analyzed using GraphPad Prism 9. The relative light unit (RLU) values recorded from uninfected cells were used to define 0% infectivity and RLU values recorded from cells infected with pseudovirus without sera or antibodies were used to define 100% infectivity. ID50 and IC50 values for sera and monoclonal antibodies, respectively were determined from the normalized data points using a [inhibitor] vs. normalized response – variable slope model.

QUANTIFICATION AND STATISTICAL ANALYSIS

GraphPad Prism 9 and Octet Data Analysis HT software v12.0 were used to analyze neutralization and binding data, respectively. Details regarding number of replicates and data analysis can be found in the respective figure legends and Method Details.

Cell Reports, Volume *42*

Supplemental information

Structural changes in the SARS-CoV-2 spike E406W mutant escaping a clinical monoclonal antibody cocktail

Amin Addetia, Young-Jun Park, Tyler Starr, Allison J. Greaney, Kaitlin R. Sprouse, John E. Bowen, Sasha W. Tiles, Wesley C. Van Voorhis, Jesse D. Bloom, Davide Corti, Alexandra C. Walls, and David Veesler

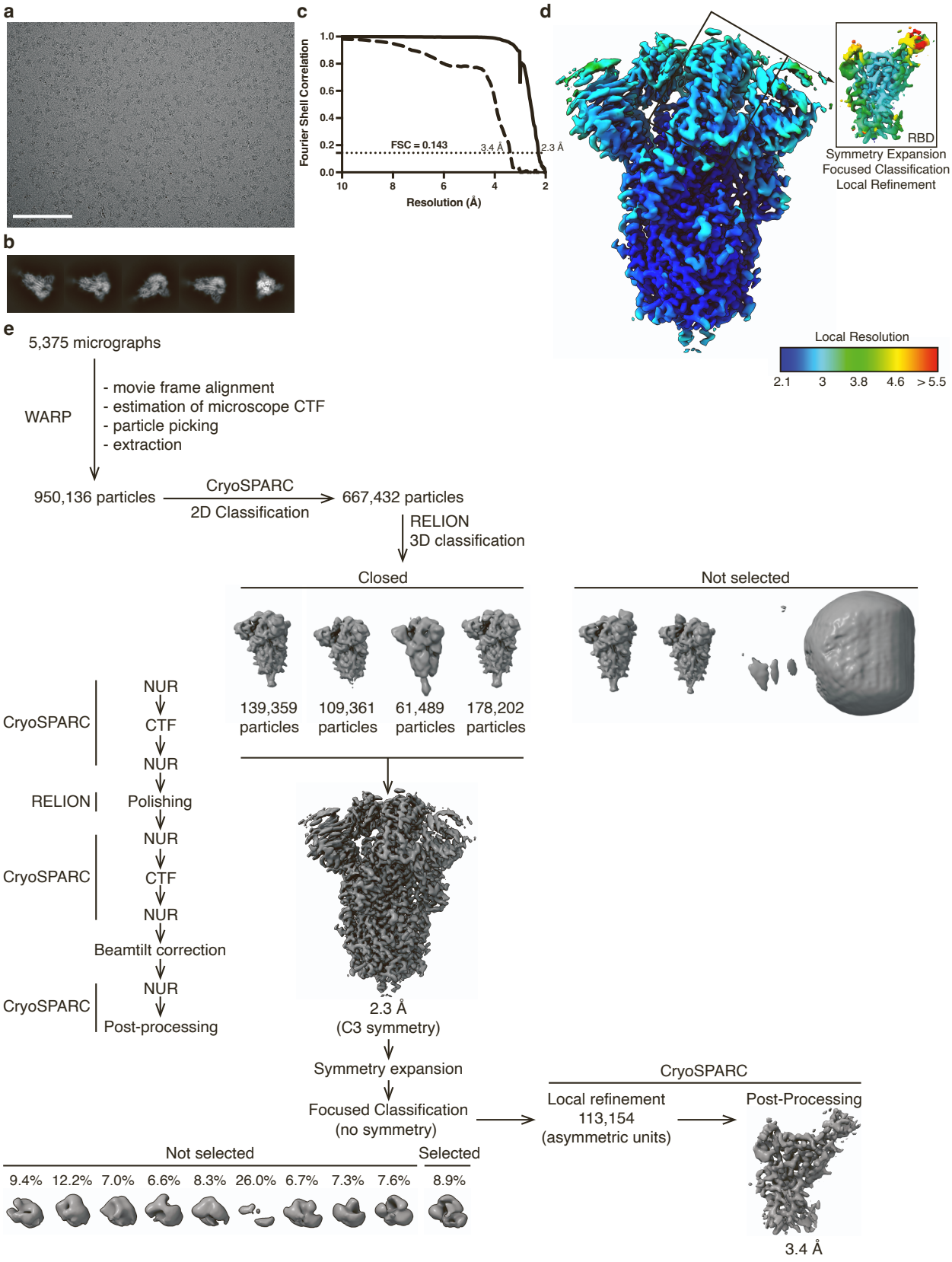
a
b
c
Fourier Shell Correlation
1.0
0.8
0.6
0.4
0.2
0.0
FSC = 0.143
3.4 Å
2.3 Å
10
8
6
4
2
Resolution (Å)
d
RBD
Symmetry Expansion
Focused Classification
Local Refinement
Local Resolution
2.1
3
3.8
4.6
>5.5
e
5,375 micrographs
WARP
- movie frame alignment
- estimation of microscope CTF
- particle picking
- extraction
950,136 particles
CryoSPARC
2D Classification
667,432 particles
RELION
3D classification
Closed
Not selected
139,359 particles
109,361 particles
61,489 particles
178,202 particles
CryoSPARC
NUR
CTF
NUR
RELION
Polishing
NUR
CryoSPARC
CTF
NUR
Beamtilt correction
NUR
CryoSPARC
Post-processing
2.3 Å
(C3 symmetry)
Symmetry expansion
Focused Classification
(no symmetry)
CryoSPARC
Local refinement
113,154
(asymmetric units)
Post-Processing
3.4 Å
Not selected
Selected
9.4%
12.2%
7.0%
6.6%
8.3%
26.0%
6.7%
7.3%
7.6%
8.9%

Figure S1. cryo-EM processing and validation for the SARS-CoV-2 E406W spike dataset; related to Figure 1 and STAR Methods**. a-b,** Representative electron micrograph (a) and 2D class averages (b) obtained for the SARS-CoV-2 E406W spike ectodomain. Scale bar: 100 nm. (c) Gold-standard fourier shell correlation curves for the closed E406W S trimer (solid line) and locally refined E406W RBD (dashed line). **d,** Local resolution calculated using CryoSPARC for the E406W S ectodomain trimer (left, unsharpened map) and the locally refined RBD (right, sharpened map). **e,** cryo-EM processing workflow.

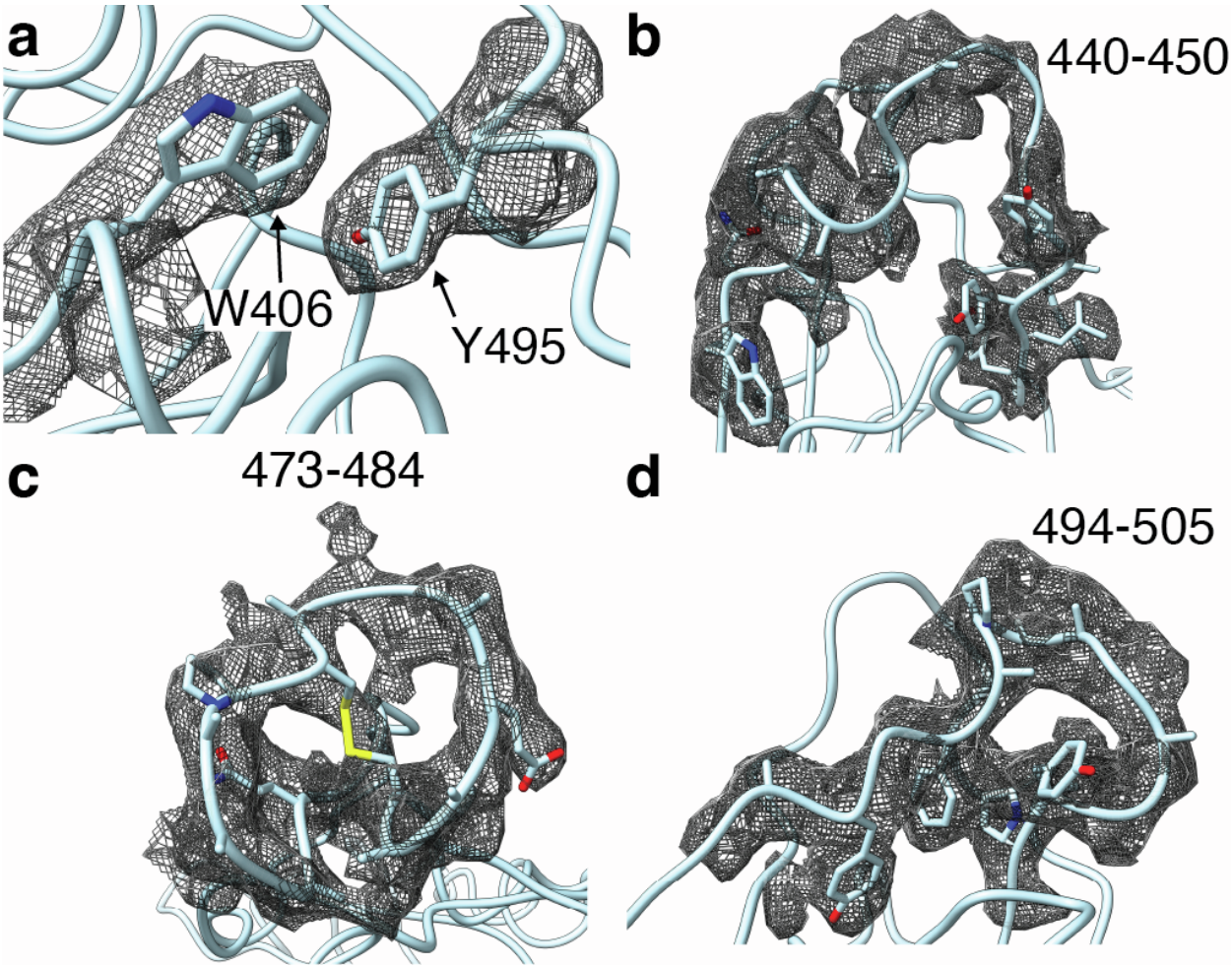

Figure S2. Support for the structural rearrangements in the W406 RBD with the locally refined cryo-EM map; related to Figure 1. Cryo-EM map, represented as a black mesh, obtained from local refinement of the RBD and the W406 RBD model compared to show the areas in which the W406 RBD diverges most significantly from the E406 RBD, including (**a**) the Y495 sidechain, (**b**) residues 440-450, (**c**) residues 473-484, and (**d**) residues 494-505.

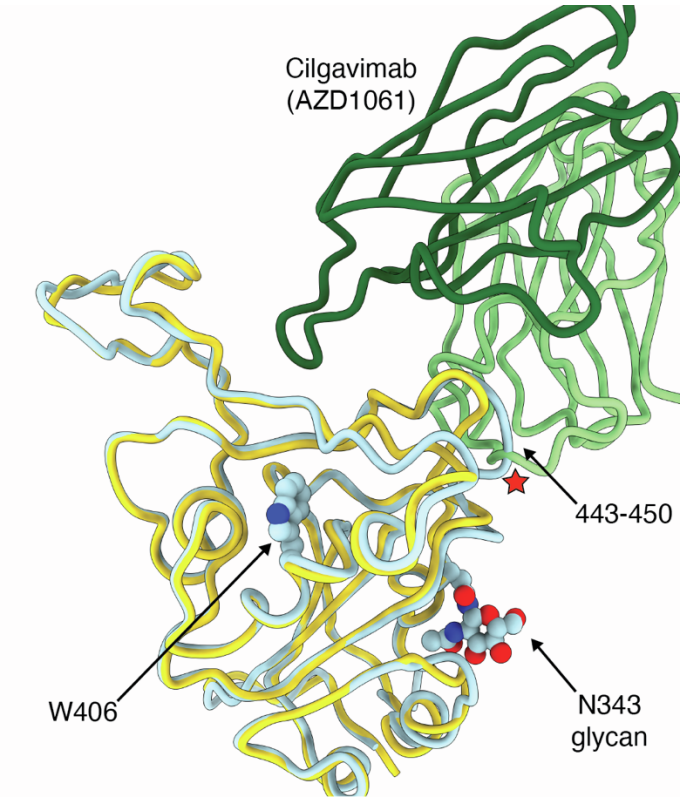

Figure S3. Repositioning of residues 443-450 in the W406 RBD interferes sterically with cilgavimab binding; related to Figure 1. Structural superimposition of the cilgavimab (AZD1061)-bound Wuhan-Hu-1 RBD (E406, gold, PBD 7L7E) and the W406 RBD (light blue). Key reorganized regions are labeled and the steric clash is indicated by a red star.

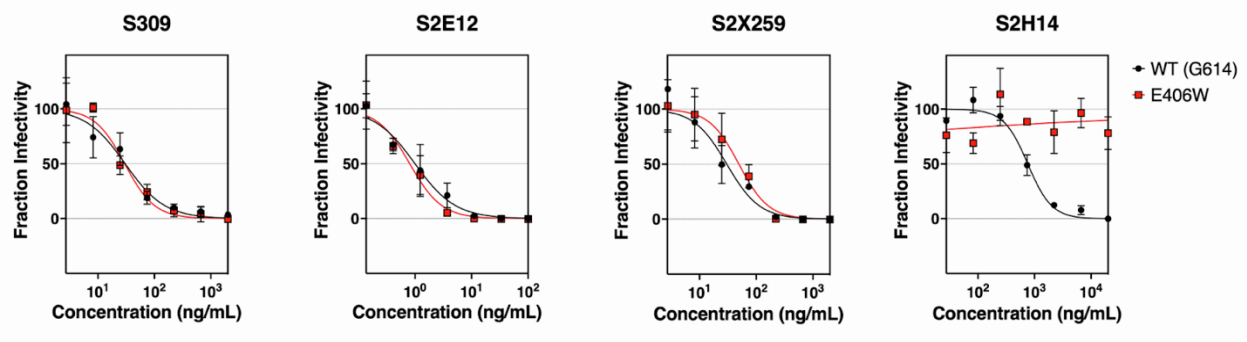

Figure S4; related to Table 1 and Figure 3. Neutralization curves for E406W/G614, shown in red, or wildtype (G164), shown in black, pseudotyped VSV using four monoclonal antibodies targeting the SARS-CoV-2 RBD. Neutralization assays were performed in triplicate and replicated twice with two batches of pseudovirus.

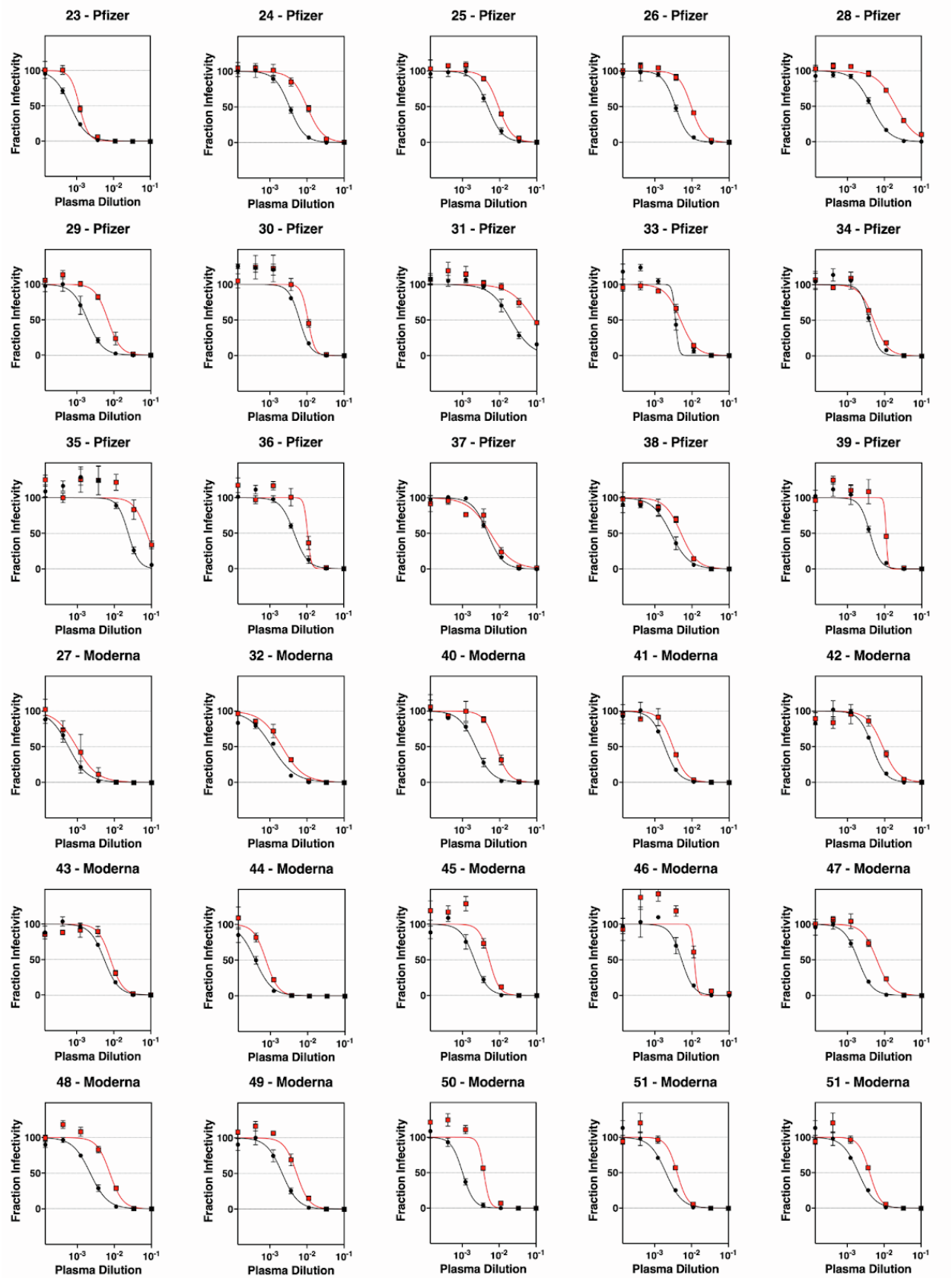

Figure S5; related to Figure 3. Neutralization curves against E406W/G614 S, shown in

red, or wildtype (G614) S, shown in black, pseudotyped VSV for 30 sera samples collected from individuals vaccinated with either Pfizer BNT162b2 or Moderna mRNA-1273 COVID-19 vaccines. Neutralization assays were performed in triplicate and repeated at least twice with at least two distinct batches of pseudovirus.

Table S1. Cryo-EM data collection, refinement and validation statistics; related to Figure 1.

	SARS-CoV-2 S E406W Ectodomain (EMDB-26056) (PDB 7TPI)	SARS-CoV-2 S E406W RBD (local refinement) (EMDB-26058) (PDB 7TPK)
Data collection and processing		
Magnification	105,000	105,000
Voltage (kV)	300	300
Electron exposure ($e^-/Å^2$)	63	63
Defocus range (μm)	- 0.1 to -2.6	-0.1 to -2.6
Pixel size (Å)	0.843	0.843
Symmetry imposed	C3	C1
Initial particle images (no.)	950,136	1,281,585
Final particle images (no.)	427,195	113,154
Map resolution (Å) FSC threshold	2.3 0.143	3.4 0.143
Map resolution range (Å)	2.2-8.9	2.8-9.1
Refinement		
Initial model used (PDB code)	7LXY	6M0J

Model resolution (Å)	2.3	3.4
FSC threshold	0.143	0.143
Map sharpening *B* factor (Å^2)	-71	-104
Model composition		
Non-hydrogen atoms	21,168	1,446
	2,862	194
Protein residues	54	1
Ligands		
B factors (Å^2)		
Protein	38.08	26.84
Ligand	21.98	23.50
R.m.s. deviations		
Bond lengths (Å)	0.012	0.012
Bond angles (°)	1.434	1.867
Validation		
MolProbity score	1.01	1.02
Clashscore	2.21	0.37
Poor rotamers (%)	0.49	0
Ramachandran plot		
Favored (%)	97.95	94.27
Allowed (%)	2.05	5.21
Disallowed (%)	0	0.52

Table S2. Binding kinetics of the RBD to human ACE2 as measured by biolayer interferometry. Values are presented as mean ± standard error; related to Figure 2.

	K_D (nM)	k_{on} ($M^{-1}s^{-1}$)	k_{off} (s^{-1})
WT	93.9 ± 3.3	1.4×10^{5}	1.2×10^{-2}
Alpha	10.9 ± 0.9	2.3×10^{5}	2.5×10^{-3}
E406W	1,335 ± 195	7.6×10^{4}	1.0×10^{-1}

Table S3. Demographic information for vaccine-elicited sera donors; related to Figure 3.

Study ID	Age	Vaccine Type	Days after second vaccination	Sex	Race	Ethnicity
23	60	Pfizer	11	M	White	Not Hispanic or Latino
24	65	Pfizer	10	M	White	Not Hispanic or Latino
25	55	Pfizer	18	M	White	Not Hispanic or Latino
26	42	Pfizer	9	F	White	Not Hispanic or Latino
27	66	Moderna	8	F	White	Not Hispanic or Latino
28	63	Pfizer	10	M	White	Not Hispanic or Latino
29	27	Pfizer	8	F	White	Not Hispanic or Latino
30	38	Pfizer	8	F	Asian	Not Hispanic or Latino
31	37	Pfizer	21	F	Black	Not Hispanic or Latino
32	36	Moderna	7	M	White	Not Hispanic or Latino
33	62	Pfizer	15	M	Pacific Islander	Not Hispanic or Latino
34	54	Pfizer	14	F	White	Not Hispanic or Latino
35	60	Pfizer	14	F	White	Not Hispanic or Latino
36	32	Pfizer	13	F	White	Not Hispanic or Latino
37	52	Pfizer	11	M	White	Not Hispanic or Latino
38	61	Pfizer	9	M	White	Not Hispanic or Latino
39	32	Pfizer	22	F	White	Not Hispanic or Latino
40	40	Moderna	20	M	White	Not Hispanic or Latino
41	64	Moderna	16	M	White	Not Hispanic or Latino
42	34	Moderna	23	F	Asian	Not Hispanic or Latino

43	22	Moderna	20	F	White	Not Hispanic or Latino
44	24	Moderna	18	F	White	Not Hispanic or Latino
45	35	Moderna	20	M	White	Not Hispanic or Latino
46	40	Moderna	24	M	White	Not Hispanic or Latino
47	55	Moderna	20	M	White	Not Hispanic or Latino
48	25	Moderna	22	M	White and Asian	Not Hispanic or Latino
49	26	Moderna	18	F	White	Not Hispanic or Latino
50	36	Moderna	27	F	Asian	Not Hispanic or Latino
51	53	Moderna	20	F	White	Not Hispanic or Latino
52	47	Moderna	21	M	White	Not Hispanic or Latino